

Contents lists available at ScienceDirect

Carbon

journal homepage: www.elsevier.com/locate/carbon



Research Paper

Carbon transformations in rapidly solidified nickel—carbon ribbon

G. Greenidge, S. Price, J. Erlebacher*

Department of Materials Science and Engineering, Johns Hopkins University, Baltimore, MD, USA



ARTICLE INFO

Article history:
Received 8 March 2021
Received in revised form
10 August 2021
Accepted 13 August 2021
Available online 17 August 2021

ABSTRACT

We report the structural transformations of carbon via the melt spinning and subsequent annealing of nickel-carbon alloys. We attained metastable solid solubility of carbon in nickel ribbon by achieving a rapid solidification rate of up to 1.6×10^6 K/s. Excess carbon atoms were found to be dissolved in the nickel lattice causing up to 1.4% strain for an alloy spun at 70 m/s tangential wheel speeds. High temperature heat treatments led to precipitation of carbon from the nickel lattice on the ribbon free surfaces but also led to growth of spherical precipitates within the nickel matrix, an effect consistent with bulk diffusion-driven Ostwald ripening. Carbon was excavated from the ribbons via chemical dissolution of the metal and characterized by electron microscopy and Raman spectroscopy. We found that the microstructure of carbon precipitated from the rapidly quenched ribbon could be tuned by varying the carbon content from 4 to 12 at. % in the precursor and annealing the ribbon at temperatures that ranged from 400 to 1200 °C. Via the step-wise variation of these two parameters, we sequentially transformed amorphous carbon nanospheres with a high BET surface area of 203 m²/g into thick, highly crystalline flakes of graphite that conformed to the shape of the as-spun ribbon.

© 2021 Published by Elsevier Ltd.

1. Introduction

The morphology of graphite precipitated from metallic melts has long been of scientific interest [1]. Commercial cast irons, one of the world's most industrially significant casting materials, contain ~2–4 wt% carbon, and their properties vary depending on the microstructure of the carbon precipitated within it. When the precipitated graphite is flake-shaped, cast iron exhibits good compressive strength but low ductility. "Ductile iron," with improved mechanical properties, was discovered in the 1940s when researchers added small quantities of impurities to the melt that converted the graphite morphology from flakes to spheroids [2].

The use of nickel and other metals as catalysts for the growth of graphitic materials has been under investigation since the 1970s [3]. In particular, the discovery of isolated graphene in 2004 [4] has led to a surge in studies investigating the synthesis of the novel material on metal substrates. Researchers have grown graphene and graphite nanocrystals by dissolving graphite powder in molten nickel and other metals at high temperatures, followed by carefully controlled cooling steps to facilitate the nucleation and growth of

* Corresponding author. *E-mail address*: jonah.erlebacher@jhu.edu (J. Erlebacher). single or multiple layers of carbon atoms on the liquid surface [5-8].

Amini and Abbaschian [9] performed a detailed study on the kinetics of this process. The authors found that graphite grows with a flake or spherical morphology depending on the supersaturation of the metallic solution and the solidification rate. They also determined that the driving force for nucleation and growth is governed by the supersaturation, that is, the difference in chemical potential between a carbon atom in a metallic solution and that atom in a crystal. Also noteworthy is their observation that high cooling rates favor the formation of graphite with a spherical morphology due to isotropic growth of both the basal and prismatic interfaces.

Alternatively, one of the most well-studied methods to grow graphene is by chemical vapor deposition (CVD), whereby carbon-containing gaseous precursors are thermally decomposed on metal foils that catalyze the formation of the single layer of graphite [10]. In both methods, the mechanism of graphene formation is similar, namely, carbon dissolution into the substrate followed by precipitation on the surface [7].

Yu et al. postulated that graphene formation on Ni foils via CVD involves the transport of vacancy-carbon complexes to grain boundaries and surfaces (which act as sinks), a process strongly dependent on the cooling technique [5]. They, therefore, studied the effect of different cooling rates on the growth of graphene

corresponding to fast (20 K/s), medium (10 K/s) and slow (0.1 K/s) cooling rates on Ni substrates exposed to precursor hydrocarbon gas for a short time. At the slowest cooling rate, no graphene was observed because the carbon atoms had sufficient time to diffuse into the bulk metal, whereas the medium cooling rate resulted in the formation of few-layer graphene. The fastest cooling rate resulted in graphite with a high concentration of defects as the quenching prevented the atoms from re-arranging into their equilibrium crystalline form. Huang and colleagues were also able to synthesize single and few-layer graphene using a rapid CVD technique and a cooling rate of 3 K/s [11].

In an attempt to develop a faster method than CVD to produce high quality graphene, Hu et al. examined rapid solidification via melt-spinning of nickel-carbon melts [12]. Invented by British scientists Strange and Pim in 1908, melt spinning has been used to manufacture sheets and ribbons of various metals [13]. In this process, a molten stream of metal impinges onto a spinning metal wheel and solidifies into a ribbon. Heat from the liquid is extracted via conduction through the wheel, leading to cooling rates that can exceed 10⁶ K/s [14]. Compared to conventional solidification methods, rapid solidification techniques can produce microstructures with fine grains (even metallic glasses), extended solid solubility and metastable phases [15].

The work performed by Hu and others shows that melt spinning is also a viable method to produce graphene. In their study, nickel alloy ingots containing less than 5 at. % carbon were ejected onto a copper wheel rotating at tangential surface speeds of 25-50 m/s. Meters-long ribbon, with thicknesses that varied between 50 and 200 um were produced: the free surfaces were found to be encased in few-layer graphene. Because the solubility of carbon in solid nickel is approximately 2 at. % at the eutectic temperature, we surmised that most of the precursor carbon did not segregate to the surface of the ribbon to form graphene and instead remained uniformly dissolved in the nickel matrix. Indeed, Nishitani and Ishihara et al. previously demonstrated that rapid solidification presented a new route to a metastable nickel-carbon precursor and that high temperature heat treatments resulted in the decomposition of these non-equilibrium phases into nickel and carbon. In other words, melt spinning leads to a supersaturated solid solution of carbon in the Ni phase and depending on the liquid undercooling, a metastable Ni₃C phase [16,17]. We aim to advance the work of these researchers by demonstrating that heat treatments can be used to control the microstructure of freestanding carbon precipitated from rapidly solidified Ni-C materials in novel ways.

In this manuscript, we present a detailed study of the morphological transformation that occurs when carbon is precipitated from melt spun nickel-carbon alloys. Overall, we find that melt spun nickel-carbon is indeed supersaturated with carbon, and that a variety of carbon morphologies can be produced by heat treatment and subsequent etching of the metal via chemical dissolution. The objective of this work is twofold: (i) to elucidate the precipitation kinetics of carbon from supersaturated melt spun Ni-C ribbon and (ii) to examine the morphological changes of carbon excavated from the rapidly solidified metal ribbon. Depending on processing conditions, carbon excavated from asspun Ni-C ribbon was found to range from amorphous nanospheres to thick graphite sheets. By varying the carbon content in the precursor and performing heat treatments on the ribbon after melt spinning, we achieved multiple and step-wise conversions of the carbon microstructure to acquire highly crystalline, thick flakes of graphite whose dimensions matched that of the precursor ribbons.

2. Experimental methods

2.1. Alloy preparation

Nickel-carbon alloy ingots were prepared by inductively melting the constituents in a water-cooled copper crucible using a 45 kW Ambrell Ekoheat ES induction system under a flowing Ar atmosphere. The precursor alloys used in the subsequent melt-spinning experiments were (measured in at. %): Ni₉₆C₄, Ni₉₂C₈, Ni₉₀C₁₀, Ni₈₈C₁₂, where the constituent Ni (99.98 wt %) was purchased from Kurt J. Lesker and graphite (99.995 wt %) from Sigma Aldrich.

2.2. Melt spinning

The components of the melt spinner (Arcast Inc.) are shown in Fig. 1 and are enclosed in a stainless steel vacuum chamber. The equipment consists of (i) a boron nitride crucible with a 3/64" diameter nozzle that was machined in-house (the crucible head was replaced every three runs or when the nozzle was abraded beyond repair), (ii) RF induction coils, and (iii) the copper wheel (300 mm diameter and 50 mm wide) that was water-cooled to 13 °C during experiments, and (iv) a collection tube for ribbon.

In a typical experiment, an approximately 20 g alloy ingot charge was inserted into the crucible, the chamber was evacuated and backfilled with purified argon to −10 psig. The charge was melted via RF induction heating using a 15 kW power supply and the temperature was monitored using a Dias Pyrospot DS 56 N pyrometer. The crucible was then lowered to a preset distance (about 1 mm) above the rotating wheel and the molten alloy was ejected via pressurized argon. The jet forms a melt pool on the cold copper surface and solidifies into a ribbon that is typically several meters in length, ~1–3 mm wide and with a thickness in the range of 20–50 μm, depending on experimental parameters. The wheel

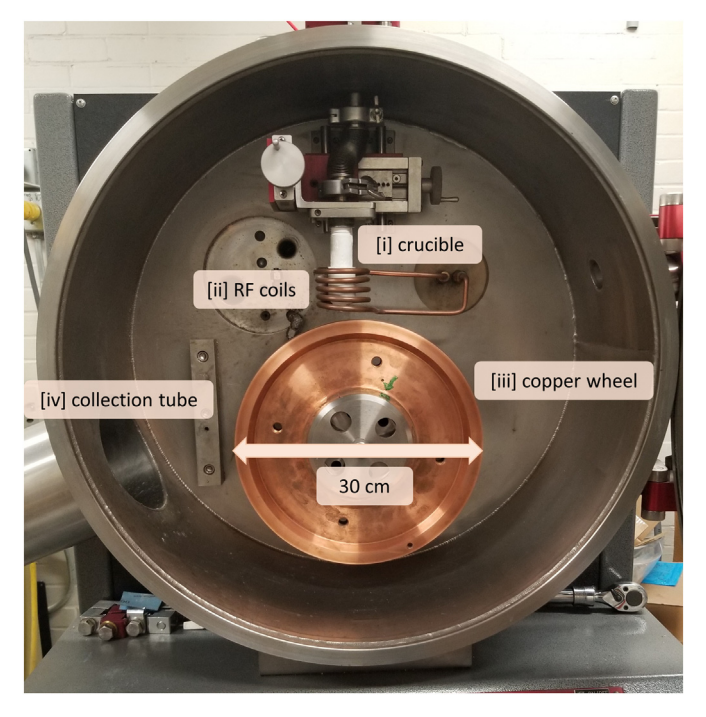


Fig. 1. (a) Photograph showing major components of the melt spinning apparatus. (i) A typical boron nitride crucible that houses the pre-cast nickel carbon ingot is shown. (ii) RF coils surround the base of the crucible and are used to melt the ingot. The melt is ejected onto the surface of (iii) the water-cooled copper wheel and solidified into ribbon that is retrieved from (iv) the collection tube. (A colour version of this figure can be viewed online.)

rotation rate was varied between 2500 and 5000 rpm, corresponding to a surface tangential speed of 40–80 m/s. Above 80 m/s, excessive sticking of the ribbon to the wheel occurred, a phenomenon discussed in detail by Liebermann and others [18,19]. Typically, the entire 20 g ingot was spun into ribbon within 5 s.

Ribbon microstructures, plan view and cross-section, were investigated using Scanning Electron Microscopy (SEM) and Transmission Electron Microscopy (TEM). Composition analysis was performed using Energy Dispersive Spectroscopy (EDS) and phase analysis was conducted via X-ray Diffraction (XRD). The wheel was prepared between each run by polishing with silicon carbide sanding sheets of incrementally decreasing grit size, and because the literature concludes that the wheel speed is the most important parameter that affects the cooling rate [20], the ejection pressure and melt superheat were kept constant and only the wheel velocity was varied.

A minimum of 3 ribbon samples were made under the same synthesis conditions. Selected samples were mounted longitudinally in epoxy, polished, and the microstructure of the ribbon cross-section was examined via SEM. Plan view SEM micrographs were obtained by mounting the ribbon horizontally on SEM stubs. Sections were removed via FIB in preparation for TEM imaging. Ribbon thicknesses were measured using a digital micrometer, and a minimum of 4 measurements were taken for each sample and averaged.

2.3. Dissolution of metal phase to excavate carbon material

Metal-carbon ribbons were immersed in 5 M HCl solution at room temperature to remove the metal phase and excavate carbon in the ribbon. The acid was filtered off using a Millipore filter and the remaining carbon material was washed with deionized water until neutral. Carbon materials were characterized using SEM, EDS, and Raman spectroscopy.

2.4. Ribbon annealing

The melt-spun ribbons with varying carbon contents were annealed in a tube furnace under a flowing Ar atmosphere (99.999%) at different temperatures: 400 °C, 800 °C, 1000 °C and 1200 °C for 60 min. To observe the effect of annealing time on the microstructure of the ribbon, $Ni_{92}C_8$ ribbon was annealed at 1000 °C for 1 min, 30 min and 240 min. After annealing, the ribbons in each of these experiments were cooled slowly at 0.06 K/s from their respective annealing temperatures to room temperature.

2.5. Characterization tools

SEM imaging was performed using a Thermo Scientific Helios G4 UC Focused Ion Beam/Scanning Electron Microscope (FIBSEM) instrument (5 kV and 10 kV) equipped with an energy dispersive spectroscopy (EDS) detector which was used for compositional analysis (See Table SI in Supplemental Information for EDS data). The FIBSEM instrument was also used to prepare samples for imaging using the Thermo Scientific TF30 Transmission Electron Microscope (TEM) instrument (300 kV). XRD was performed with a Bruker D8 Focus diffractometer with a CuK α source. Raman spectroscopy was carried out using a Horiba LabRam Evolution Raman microscope with a 532 nm laser line and a 100 μ m spot size. 3-point BET surface area measurements were performed commercially using a Micrometrics TriStar II 3020 instrument.

3. Results and discussion

3.1. Microstructural evolution of melt-spun ribbon

Conventional solidification typically proceeds at cooling rates lower than 100 K/s and generally results in phases and microstructures predicted by equilibrium thermodynamics [21]. However, melt spinning is a far-from-equilibrium cooling technique where solidification rates between $10^4 - 10^7$ K/s are encountered [15]. As a result, phases and microstructures that are favored kinetically instead of thermodynamically may evolve. The equilibrium Ni-C phase diagram is a simple eutectic with a eutectic composition and temperature of Ni₉₂C₈ and 1326 °C, respectively, and a maximum solubility of carbon in the nickel phase of ~2 at. % at the eutectic temperature. Fig. 2(a) shows a comparison of the microstructure of a Ni₉₂C₈ ingot conventionally cooled in an induction furnace and the cross-section of melt spun ribbon of the same composition. The lighter regions are the Ni-rich phase and the darker regions are carbon particles embedded in the metal. As expected, the conventionally cooled ingot shows visible carbon precipitates (by which we mean crystalline - though potentially

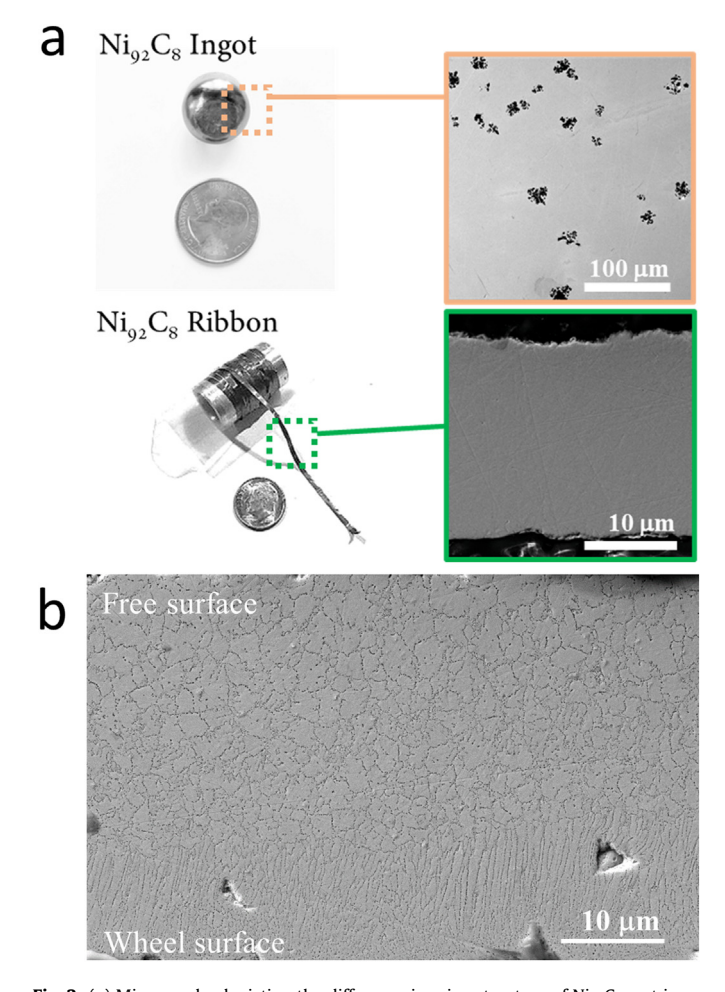


Fig. 2. (a) Micrographs depicting the difference in microstructure of $Ni_{92}C_8$ cast in an induction furnace and that of melt-spun ribbon of the same composition. In the conventionally cooled ingot, the microstructure shows that Ni (light grey background) and C (black precipitates) have phase separated. However, a homogeneous single phase is observed for the melt-spun ribbon. (b) SEM micrograph of a cross-section of $Ni_{88}C_{12}$ ribbon spun at 48 m/s showing a typical melt-spun microstructure. Carbon precipitates highlight the evolution of the grain structure from the wheel surface (ribbon surface that was in contact with the wheel) to the ribbon free surface. (A colour version of this figure can be viewed online.)

highly defected — precipitates consisting of graphitic carbon), indicating phase separation between Ni and carbon. In contrast, the melt-spun ribbon shows a featureless, uniform Ni phase with no visible carbon precipitation, suggesting that melt spinning results in a metastable solid solution of carbon in the metal.

In melt spinning, a molten alloy jet is ejected on a rotating metal wheel substrate to form a ribbon or strip. A melt puddle is formed on the substrate from which quenched ribbon is continually expelled. The wheel surface acts both as a heat sink and heterogenous nucleation site for the growth of solid phases. Typically, solidification begins in the form of fine, equiaxed crystals and extends laterally until the contact surface is covered. From this initial chill zone, columnar grains grow in the direction parallel to the thermal gradient, i.e., normal to the ribbon surface. In Ni alloys, the preferential growth direction of the columnar grains is the [100] direction [22]. With sufficient cooling rates, the early stage of columnar solidification is partitionless; that is, the solidification velocity is faster than the diffusion of solutes, which become trapped in the solid phase. Where c_S is the solute concentration in the solid and c_L is the solute concentration in the melt, the equilibrium partition coefficient $k = c_S/c_L$ is generally less than unity but can approach k = 1 in rapid solidification processes [23], and the equilibrium solid solubility can be greatly exceeded. As the solidification front advances from the contact surface to the free surface, the latent heat of solidification is released, reducing the thermal gradient and the interface velocity. When solidification is no longer partitionless, the microstructure of the ribbon transitions into a cellular configuration with much larger grains.

As shown in Fig. 2(b), the solidification microstructure of $Ni_{88}C_{12}$ follows the expected behavior of melt spun metals, transitioning from fine equiaxed crystals to columnar to larger cellular grains [22]. As discussed below, most of the carbon is dissolved in the solidified nickel matrix; however, there is a small amount of carbon that segregates to grain boundaries, allowing the microstructural features to be highlighted.

Many experimental parameters affect the cooling rate, including the melt superheat, the ejection gas pressure, wheel material and its surface finish, and the wheel velocity. Increasing the wheel velocity increases the cooling rate due to improved thermal contact between the ribbon and the substrate, but also because it results in a decrease in ribbon thickness [21]. Thickness has been described as the most important feature of melt-spun ribbon that determines the cooling rate, where the average cooling rate increases approximately as the inverse square of ribbon thickness for ideal cooling [20,22]. The cooling rate is directly proportional to the wheel velocity and inversely proportional to the square of ribbon thickness.

We investigated the relationship between wheel speed and ribbon thickness to determine the optimal conditions under which continuous, uniform, thin, rapidly solidified ribbons were produced. We kept constant the surface finish, melt superheat, and ejection pressure and varied only the wheel velocity and carbon content. Fig. 3 shows this observed relationship, where ribbon thickness (h) decreases with wheel velocity (v) as

$$h \propto k / v^{0.6} \tag{1}$$

where k is a constant. The experimentally derived exponent reported here is in close agreement with the equation derived by Gillen and colleagues [24]:

$$h \propto Q/v^{2n} \tag{2}$$

where Q is the volumetric flow rate and n is in the range 0.3–0.4. Specifically, n was found to be 0.35 for Ni-5wt%Al. Jones et al. proffered a slightly different variation of Gillen's equation in which

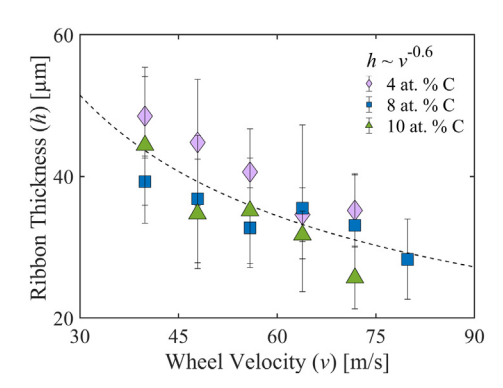


Fig. 3. Ribbon thickness (h) vs. tangential wheel velocity (ν) for different carbon fractions: Ni containing 4 at. % C (purple diamonds), 8 at. % C (blue squares), 10 at. % C (green triangles). Error bars represent a standard deviation. (A colour version of this figure can be viewed online.)

$$h \propto Q^n / v^m \tag{3}$$

where *n* and *m* are typically 0.2 and 0.8, respectively [21], which is still in good agreement with the relationship reported in this work. Gillen also derived a linear equation relating wheel speed to cooling rate that is independent of other melt spinning experimental parameters and the alloy material:

$$T = a_4 v \tag{4}$$

where T is the cooling rate and a_4 is a constant of proportionality equal to 1.2×10^4 K/s. Using Eq. (4), we estimate the cooling rates achieved in the melt spinning of nickel-carbon alloys in this work were in the range $9.6 \times 10^5 - 1.9 \times 10^6$ K/s.

The effect of thermal annealing on the ribbon microstructure was also investigated. TEM images comparing as-prepared ribbon with ribbon annealed at 1000 °C are shown in Fig. 4. The TEM micrograph of a sample before annealing shows a homogenous region of micron sized Ni grains with no obvious carbon precipitates observable within the resolution of the image. In contrast, after annealing, Ni grains have grown and carbon precipitates are also evident; the polygonal outline of a graphite precipitate is shown in the inset.

The evolution of the nickel-carbon XRD patterns in response to annealing follows. The data labeled (i) in Fig. 5 shows the diffraction pattern of melt spun pure Ni ribbon. The XRD pattern of as-spun Ni₉₂C₈ ribbon is also shown, labeled (ii). Compared to pure Ni, the (111) peak in this sample splits, where the higher intensity peak is shifted to smaller 2θ due to a 1.2% lattice expansion, consistent with supersaturation of carbon in the interstitial sites of the nickel lattice due to the high cooling rates. The peak shoulder at the larger 2θ value represents unstrained Ni, indicating that phase separation between Ni and supersaturated Ni has occurred. The XRD pattern of Ni₉₂C₈ ribbon annealed at 1000 °C for 1 h is shown as (iii) and indicates the Ni lattice peak has returned to the unstrained position. Therefore, the Ni lattice strain is relieved during carbon precipitation. This observation is confirmed by the appearance of the precipitated graphite (002) peak. The appearance of the metastable Ni₃C phase is not shown in Fig. 5 but evidence of its formation is discussed in the supplemental section. Details of annealing the nickel-carbon ribbon will be further discussed in Section 3.2.

3.2. The effect of annealing temperature and time on carbon precipitation

To re-iterate, as-spun ribbons generally accommodated a large

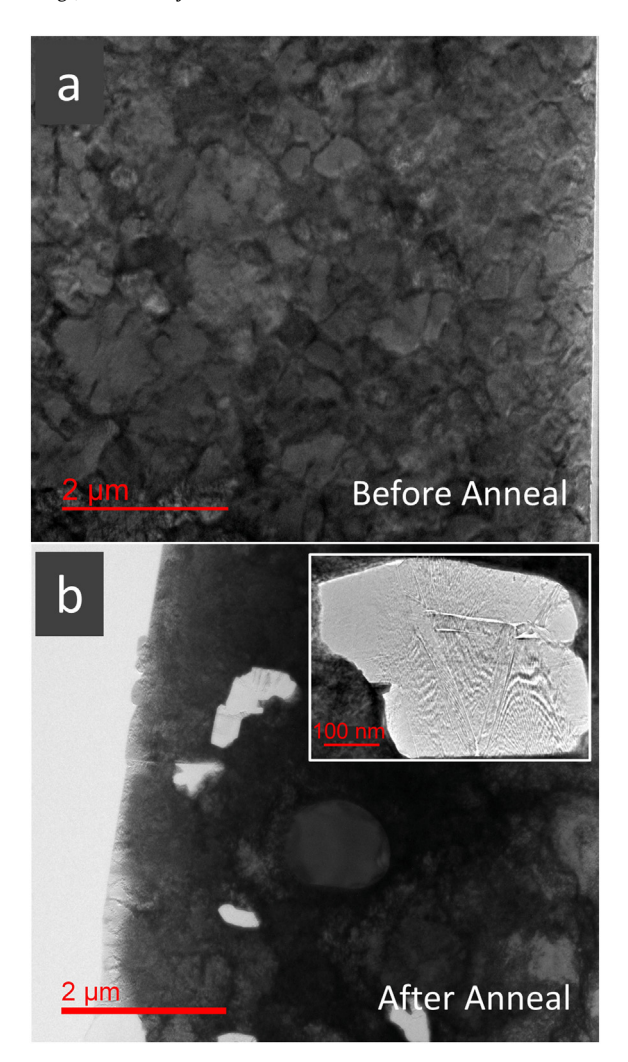


Fig. 4. Bright field TEM micrographs of $Ni_{92}C_8$ ribbon spun at 48 m/s. (a) Image taken before annealing shows micron-sized grains and no evidence of carbon precipitation. (b) Image of ribbon annealed at 1000 °C for 1 h shows grain growth and (inset) the presence of large graphite particle (light contrast) embedded in the Ni matrix. (A colour version of this figure can be viewed online.)

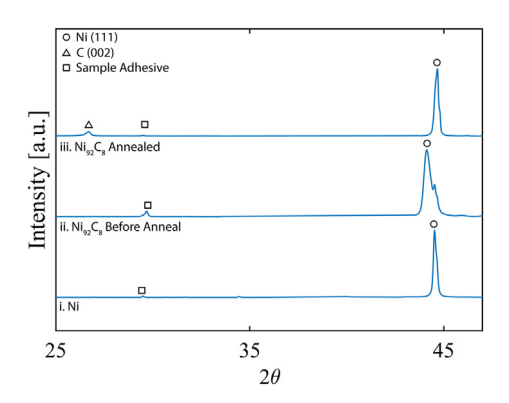


Fig. 5. XRD patterns showing the effect of annealing on the Ni peak positions in melt-spun ribbon prepared under the same conditions. All samples were melt spun at 48 m/s. (i) Shows unstrained Ni (111) peak, (ii) Shows phase separation between a strained Ni (111) peak (shifted to a smaller 2θ indicating lattice expansion) and an unstrained Ni (111) peak that appears as a shoulder. (iii) Shows that annealing relieves the lattice strain as the Ni (111) peak returns to the unstrained position. Additionally, the graphite (002) peak appears. (A colour version of this figure can be viewed online.)

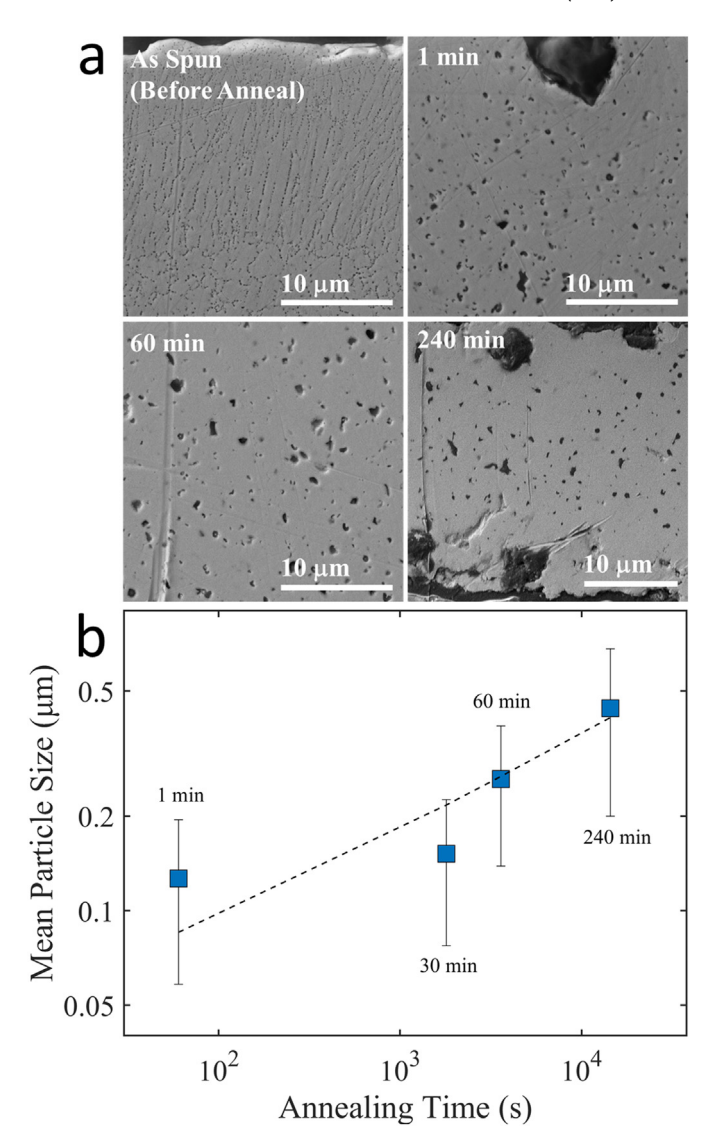


Fig. 6. (a) SEM micrographs (cross-section) showing growth of carbon precipitates in $Ni_{92}C_8$ ribbon spun at 48 m/s and annealed at 1000 °C for increasing times. (b) Log-Log plot of mean particle size as a function of time. The dashed line shows a power law fit with n=1/3. (A colour version of this figure can be viewed online.)

quantity of carbon within the grains, either supersaturated in the nickel matrix or as metastable Ni₃C, where the ribbon appeared as uniform and featureless within the resolution of the scanning electron microscope, such as shown in Fig. 2(a). However, as Fig. 2(b) shows, we also commonly observed some carbon precipitation at Ni grain boundaries in some ribbons. This occurrence was more likely to be observed in material containing higher amounts of carbon, and to a lesser extent, in select regions of ribbons containing lower carbon fractions. Because ribbon thickness can vary point to point within the sample, the cooling rate can be attenuated, leading to C segregation in the Ni grain boundaries even in ribbons with low carbon fractions. After annealing, however, C precipitates were uniformly dispersed throughout the matrix, no longer distinctly outlining Ni grains.

We now turn to the question of the morphological evolution of carbon precipitated from the ribbons which coarsen as a result of a thermal anneal. It seems reasonable to consider that growth of precipitates is controlled by an evaporation/condensation mechanism wherein carbon atoms dissolve ("evaporate") from

precipitates, diffuse down chemical potential gradients through the bulk of the nickel matrix, and re-attach to other precipitates. To date, we know of no study that suggests whether the rate limiting step in the nickel-carbon system is bulk diffusion or attachment/detachment at precipitates, and the situation is made more complex here by the presence of grain boundaries and surfaces that may act as short-circuit diffusion pathways. We emphasize that a study of precipitates embedded in a nickel matrix is fundamentally different than a study of graphitization of particles excavated from carbon, as graphitization does not generally involve long-range transport of carbon atoms.

The temporal evolution of carbon coarsening in $Ni_{92}C_8$ ribbon was first examined by performing 1000 °C isothermal heat treatments at varying times: 1 min, 30 min, 60 min and 240 min. This step was followed by cooling and cross-sectioning for microscopy; the cooling rate was kept constant for all experiments. Examples of

SEM micrographs used to measure particles sizes are shown in Fig. 6(a). For each annealing time, a minimum of two micrographs of the same magnification were analyzed by performing thresholding followed by measuring particles sizes with circularity from 0 to 1 using the image processing software ImageJ. The collection of particle sizes from these images were averaged to report a mean particle size.

It is clear from Fig. 6 that the average particle size has grown from initially submicron particles to particle sizes as large as 5 μ m after the 4 h anneal. In particular, in the 240 min micrograph, there are larger precipitates near the geometric surface. Surrounding each is a region missing carbon particles – a denuded zone often seen in coarsening studies. Generally, precipitate coarsening is governed by the power law $d \propto t^n$, where d is the average precipitate size, t is the annealing time and n is an exponent that varies depending on the coarsening mechanism. The Lifshitz-Slyozof-

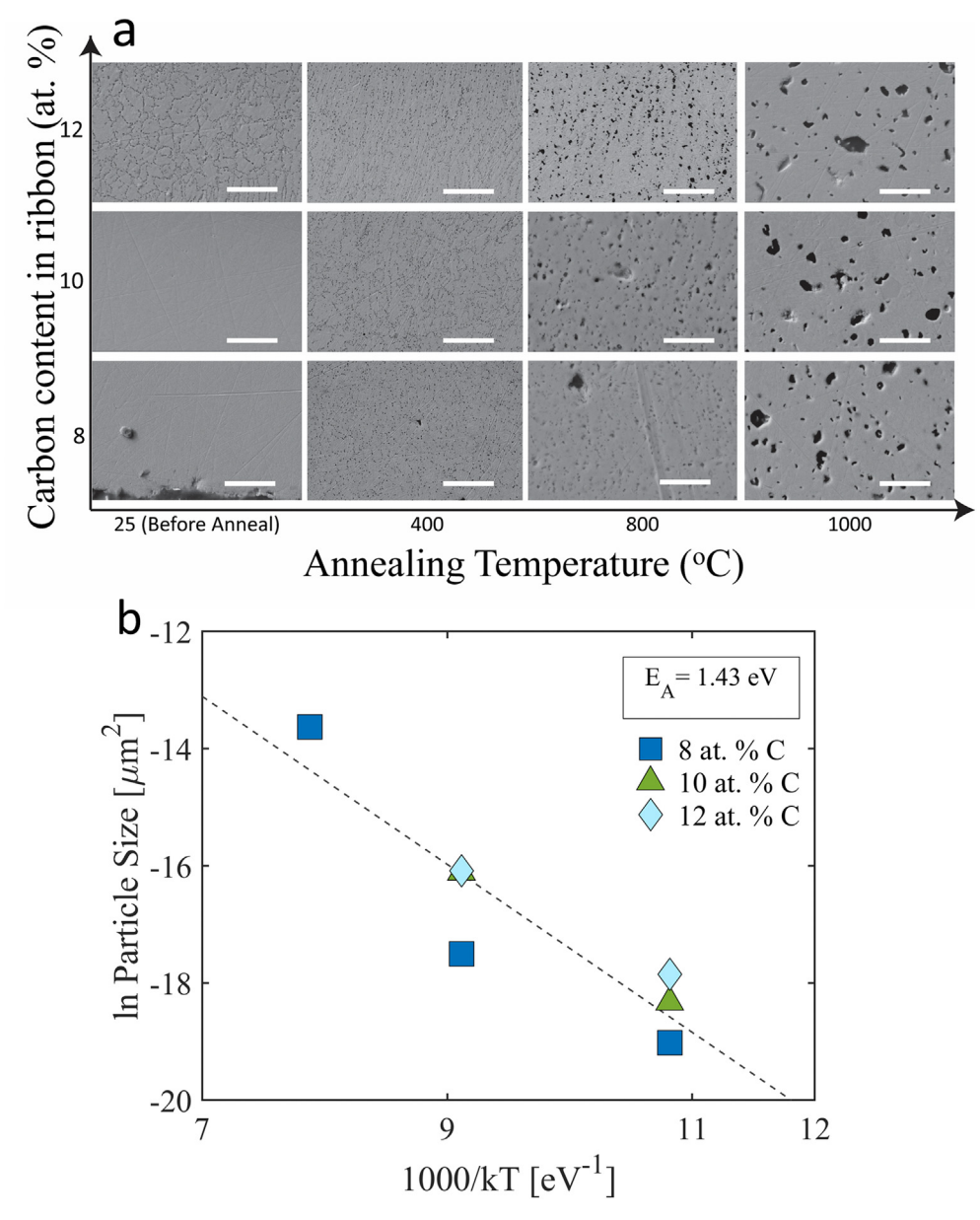


Fig. 7. (a) Microstructural variation of melt-spun Ni—C ribbon (cross-section) spun at 48 m/s with varying carbon content and annealed at different temperatures. Scale bars are 5 µm. (b) Plot of average carbon particle size in ribbon vs. annealing temperature for Ni—C ribbon of varying carbon fractions: Ni containing 8 at. % C (dark blue squares), 10 at. % C (green triangles) and 12 at.% C (light blue diamonds). The activation energy of 1.43 eV is consistent with bulk diffusion of carbon in Ni. (A colour version of this figure can be viewed online.)

Wagner (LSW) theory of Ostwald ripening [25,26] models the kinetics of precipitate growth from supersaturated solid solutions and has been extended to describe coarsening in rapidly solidified materials [27–29]. LSW theory predicts that n=1/3 for diffusion-limited coarsening [30,31]. The driving force for this process is a reduction in surface area where large particles grow at the expense of smaller ones. A plot of mean particle size vs. annealing time is shown in Fig. 6(b), with an n=1/3 power law relationship shown by a dashed line, showing good agreement between the data and model.

To further elucidate the mechanism of precipitate coarsening, ribbons were examined after a fixed annealing time but at multiple annealing temperatures and carbon content. Micrographs of representative samples are shown in Fig. 7(a). An increase in the annealing temperature led to an increase in the size of the carbon precipitates and a reduction in the number density of precipitates. Regardless of the mechanism dominating coarsening, the average particle size should be proportional to a kinetic factor exhibiting Arrhenius kinetics, either diffusion coefficient D in diffusion-limited kinetics or an attachment/detachment rate k_d , and the particle size data for the annealing temperature range of $800-1200~^{\circ}\text{C}$ plotted in Fig. 7(b) does indeed exhibit Arrhenius type behavior. The activation barrier, 1.43~eV, is consistent with other measurements of carbon diffusion in Ni above $600~^{\circ}\text{C}$, which was found to be in the range 1.42-1.52~eV [32].

Because the observations about particle coarsening are consistent with Ostwald ripening and the measurement of the activation barrier is consistent with the bulk diffusion of carbon in nickel, it is reasonable to conclude that the mechanism of carbon precipitation and morphological evolution during coarsening is dominated by bulk diffusion of carbon in the background nickel lattice, and not limited by dissolution of carbon from the precipitates.

3.3. The microstructural evolution of freestanding carbon

Here we focus on the structure of the carbon materials excavated from nickel-carbon alloys by chemical dissolution of the metal in hydrochloric acid. Fig. 8 summarizes the evolution of the carbon microstructure as a function of annealing temperature and the carbon content in the precursor ribbon. Carbon obtained from as-spun Ni-C ribbon with a low carbon content exists as amorphous spheres; that is, the carbon exhibited no long range order in the arrangement of carbon atoms. By increasing the ribbon annealing temperature, shown on the horizontal axis, the morphology of the freestanding carbon transformed into high aspect ratio carbon flakes. Fig. 8 also shows that increasing the carbon content in the precursor ribbon, shown on the vertical axis, is correlated with a conversion of the morphology from nanospheres to flakes. By increasing both these parameters simultaneously, that is, by annealing a ribbon with a high initial carbon content at a high temperature, we achieved the conversion of the amorphous nanospheres to large area highly crystalline graphite flakes (Crystallography Open Database COD ID 1011060). By the step-wise variation of these two parameters, we can incrementally transform the microstructure of carbon synthesized by melt spinning Ni-C alloys. The mechanisms of these transformations are discussed in further detail in the subsequent sections.

3.3.1. Microstructure of precursor carbon material

The structure of the commercially acquired graphite used in the precursor alloy was thick multi-layer flakes. This material was converted into spheroids and flakes when excavated from a nickel-carbon ingot prepared by induction melting and conventional cooling - structures that are typical of graphite precipitated from metallic melts [6,33]. The transformation is shown in Fig. 9.

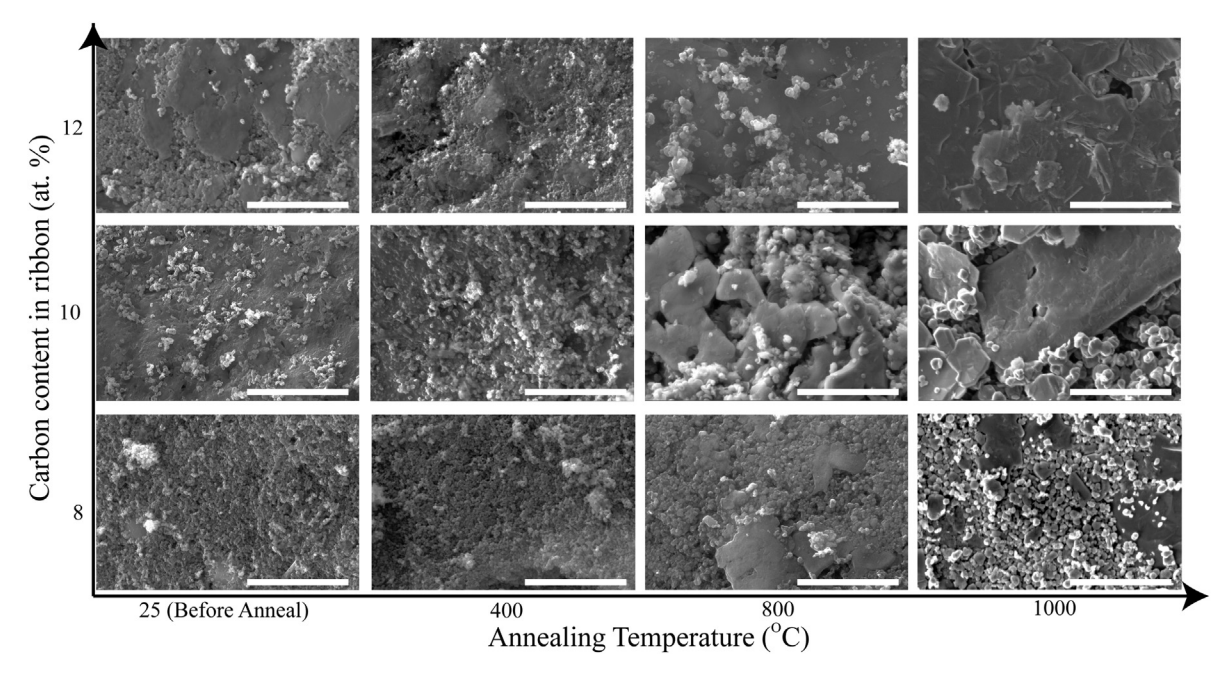


Fig. 8. SEM micrographs showing the microstructural variation of carbon excavated from melt-spun ribbon spun at 48 m/s as a function of annealing temperature and carbon content in the precursor ribbon. Scale bars are 4 μ m. As spun ribbon with a low carbon fraction (8 at. %) exhibits the structure of carbon nanospheres (bottom left). Increasing the ribbon annealing temperature or the initial carbon content in the ribbon leads to the conversion of nanospheres into flakes. By increasing both parameters simultaneously, that is, by annealing a ribbon with a high initial carbon content at a high temperature, we achieved the conversion of the amorphous nanospheres to large area graphite flakes.

3.3.2. Microstructure of carbon excavated from as-spun ribbon

Fig. 10 shows the SEM micrographs of carbon obtained by the chemical etching of the Ni phase from as-prepared Ni₉₂C₈ meltspun ribbon, i.e., without annealing. The elemental composition of the material was analyzed via EDS and is summarized in Table S1 in the Supplementary Section. Fig. 10 (a) and (b) show that thin flakes, electron transparent to 10 kV, were present in small quantities. Since no plate-like structures were present within the crosssection of melt-spun ribbon, we postulate that the observed carbon sheets precipitated at the ribbon surface, a finding that corroborates the results found by Hu et al. that graphene grows on the surfaces of melt spun ribbon [3]. The most prevalent microstructure observed were sub-micron sized nodules that either existed as separate nanoparticles or a more complex morphology consisting of clusters of particles, shown in Fig. 10 (c) and (d). The particle sizes are on the same order of magnitude as the precipitates found embedded in the nickel grain boundaries, so it is likely that is one location from which they originated. However, because the grain boundary precipitates cannot account for the quantity of carbon excavated in this case, it is reasonable to assume that another origin of the nanospheres was carbon distributed in the Ni bulk.

Raman spectroscopy was utilized to analyze the crystallinity of the fabricated material. The ratio of intensity of the D band to the G band, I_D/I_G , provides information on the defect concentration and crystallize size in disordered graphite and on the size of aromatic

clusters in amorphous carbon [34–37]. The carbon from as-spun ribbon exhibited characteristic features of amorphous carbon: broad G and D peaks and a low 2D band intensity. The high I_D/I_G ratio of 0.9 is indicative of large aromatic clusters. The BET surface area for carbon obtained from as-spun (before annealing) rapidly solidified Ni₉₂C₈ ribbon was measured to be 203 m²/g.

Increasing the carbon content in the ribbon resulted in an increased thickness of the graphite flakes; the growth front of graphene layers can clearly be identified on the surface as shown in Fig. 11. This observation indicates that controlling the carbon content of the precursor alloy may allow us in the future to tune the number of layers of graphene produced, consistent with Hu's observations [12].

3.3.3. Microstructure of carbon excavated from annealed ribbon

The resultant microstructure of carbon embedded in the Ni matrix after ribbon annealing was shown in Fig. 4; the TEM micrograph highlighted the polygonal outline of the graphite crystals, signaling the crystallization of carbon within the grains due to thermal treatment at 1000 °C. Additionally, annealing nickel-carbon ribbon promoted the precipitation of graphite on the ribbon free surfaces, as depicted in Fig. 12, where the plan view of $Ni_{88}C_{12}$ ribbon before and after annealing at 1000 °C is shown. This observation is consistent with a reduction in the density of carbon precipitates that speckle the interior of the

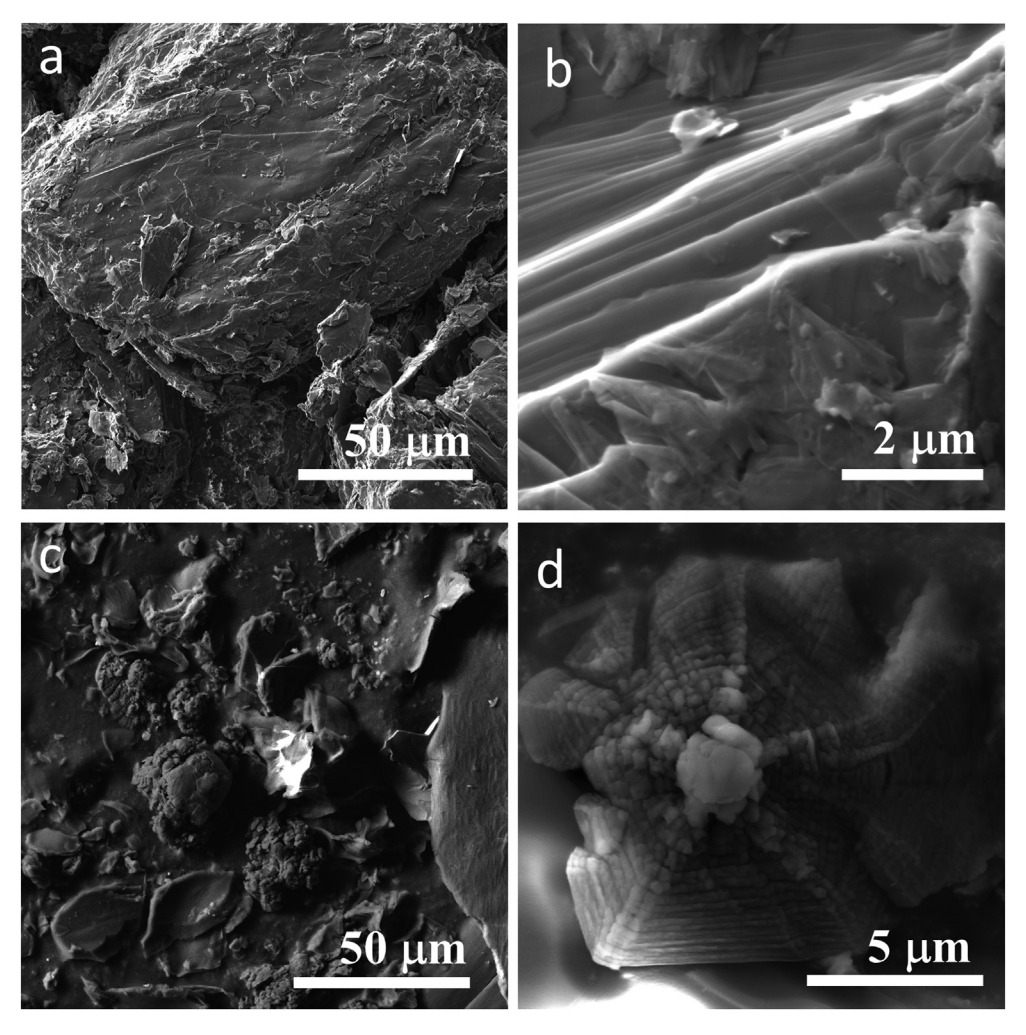


Fig. 9. (Top) (a) and (b) Commercially prepared graphite used to prepare precursor Ni—C ingots for melt-spinning; (Bottom) (c) and (d) Carbon flakes and spheroids collected by chemical dissolution of Ni from conventionally cooled Ni—C ingots prepared by induction melting.

ribbon, as well as the reduced quantity of nanospheres fabricated by excavating carbon from the ribbon. Instead, increasing the annealing temperature of the ribbon resulted in an increase in the prevalence of the high aspect ratio graphite flakes retrieved after etching the Ni matrix. Increasing the initial carbon content in the ribbon also led to the same observation: the samples that contained the highest atomic fraction of carbon (Ni $_{88}C_{12}$) and were annealed at 1000 $^{\circ}C$ for 1 h produced carbon materials consisting of large graphite flakes, hundreds of microns wide (equal to the width of the ribbon) and about 1 μm thick, and almost devoid of spherical nodules.

Raman characterization of the freestanding carbon microstructure as a function of ribbon annealing temperature is shown in Fig. 13. Table 1 also outlines the effect of annealing on the Raman spectra of carbon obtained from melt-spun ribbon. Annealing at 400 °C has little effect on increasing the crystallinity of the carbon material compared to the sample that was not annealed, consistent with other reports that 400 °C is too low of a temperature to initiate significant graphitization [38]. However, corresponding to the increase in annealing temperature, the I_D/I_C ratio decreased from 0.9 for carbon annealed at 400 °C to 0.3 for carbon annealed at 1000 °C, indicating that the thermal treatments resulted in a reduction in defect density, increase in crystallite size, and ultimately, enhanced graphitization of the

material. The I_{2D}/I_G ratio also increased from 0.31 to 0.65, signaling a resultant increase in the number of graphene layers present in the material. Similar transformations of carbon from amorphous to crystalline by increasing the annealing temperature have been well documented in the literature [39–41].

We postulate that supersaturation of the Ni lattice leads to carbon atoms being dispersed throughout the metal's interstitial sites. The carbon from the as-spun ribbon lacks crystallinity and evolves as sub-micron sized nodules — approximately the same shape and size as they were in the ribbon. Annealing, however, allows for carbon diffusion, which led to the growth and graphitization of flakes on the free surfaces of the ribbon.

It is interesting to consider the utility of the carbon materials fabricated here in the context of carbon fiber manufacture. Carbon fiber usually consists of graphitic crystal threads a few microns in diameter, with a microstructure in which the graphene planes are aligned parallel to the axis of each thread so that the strong direction is along the axis of the thread. Nominally, the microstructure of carbons produced here is similar — microns-wide graphite sheets oriented with the strong axis in the plane of the ribbon. Although the length of the flakes produced here is much shorter than those in carbon fiber, it is easy to imagine that directional precipitation and crystal growth can be induced if the ribbons were to be pulled through a hot zone rather than

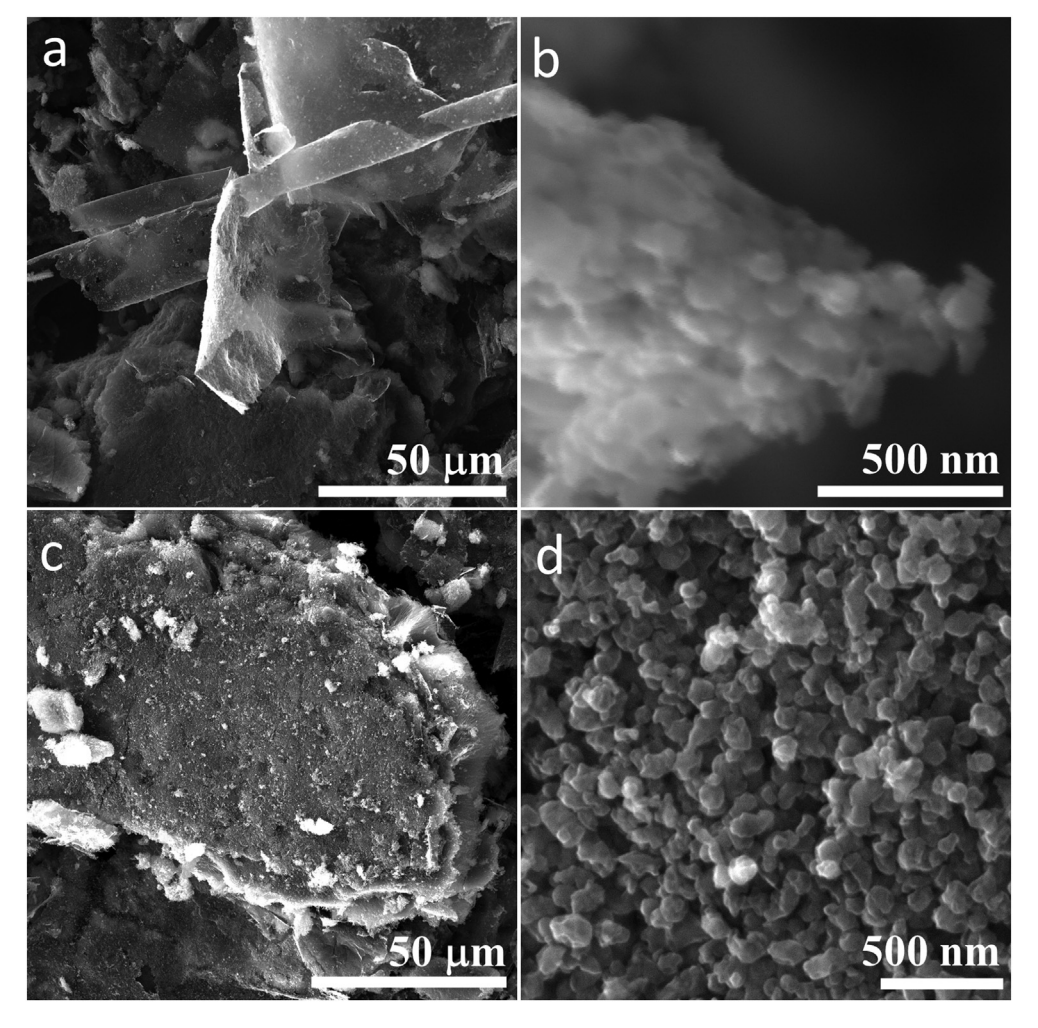


Fig. 10. Carbon etched from $Ni_{92}C_8$ melt-spun ribbon before annealing shows two types of morphologies (a) Thin carbon flakes comprised of clusters of nanometer sized carbon particles. (b) The structure shown in (a) is magnified. (c) A large carbon "slab" that is 10 μm thick and over 100 μm long. (d) At higher magnification, the slab is observed to be comprised of clusters of submicron sized particles.

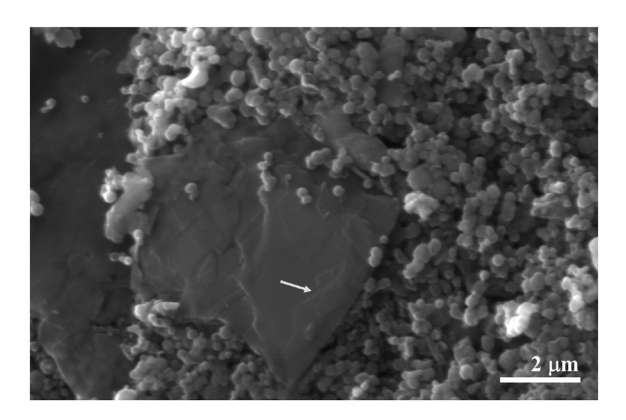


Fig. 11. Carbon from $Ni_{88}C_{12}$ melt spun ribbon before annealing showing growth front of graphene layers.

homogeneously annealed, and this should lead to very long graphite crystals. Assuming these may be spun into fiber with a suitable binder (we have not produced enough material to perform this test), this approach may be a more benign method to produce carbon fiber precursors from a life-cycle approach, as it is well-known that carbon fiber produced from polymeric precursors is an energy and resource intensive process, leading to significant emissions during the oxidation and graphitization cycles at high temperature [43].

4. Conclusions

We report the ability to melt spin nickel-carbon alloys with a carbon fraction up to 12 at. % using a water-cooled copper roller rotating at speeds between 40 and 80 m/s. Extended solubility of carbon in the Ni was confirmed by measuring Ni lattice strain using X-ray diffraction. High temperature heat treatments led to precipitation of carbon from the nickel lattice on the ribbon free surfaces but also led to the subsequent growth of the precipitates within the nickel matrix via bulk diffusion-driven Ostwald ripening. From the rapidly solidified ribbon, carbon was excavated via chemical dissolution of the metal to reveal freestanding carbon materials. We evaluated changes in carbon microstructure as a function of precursor carbon content and annealing the Ni—C ribbon. We

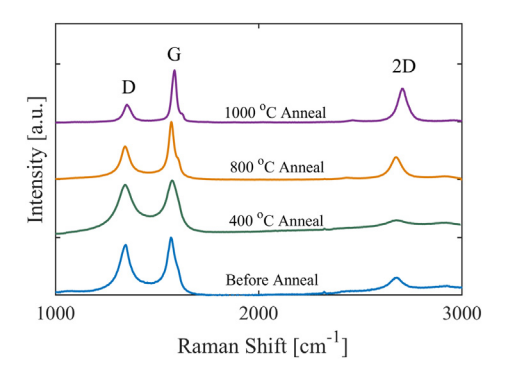


Fig. 13. Raman spectra showing increasing graphitization of carbon with increasing annealing temperatures. (A colour version of this figure can be viewed online.)

observed that the morphology of the carbon materials could be adjusted sequentially by varying these two experimental parameters. As-spun ribbon (undergoing no heat treatment) with a low carbon content will lead to the formation of high surface area amorphous carbon nanospheres and few-layer graphene. By increasing the carbon content and/or the annealing temperature, the number of nanospheres was decreased and replaced by graphite flakes. The thickness and crystallinity of these flakes can also be controlled by these experimental variables. After a high temperature heat treatment at 1000 °C, Ni₈₈C₁₂ ribbon produced thick graphite flakes from carbon material precipitated on the surfaces of the ribbon.

CRediT authorship contribution statement

G. Greenidge: Formal analysis, Writing — original draft, made samples, took measurements, analyzed data, and wrote the first draft of the manuscript. **S. Price:** assisted Greenidge. **J. Erlebacher:** Writing — review & editing, came up with the idea for the study, managed the research project, and edited the manuscript.

Declaration of competing interest

The authors declare that they have no known competing financial interests or personal relationships that could have appeared to influence the work reported in this paper.

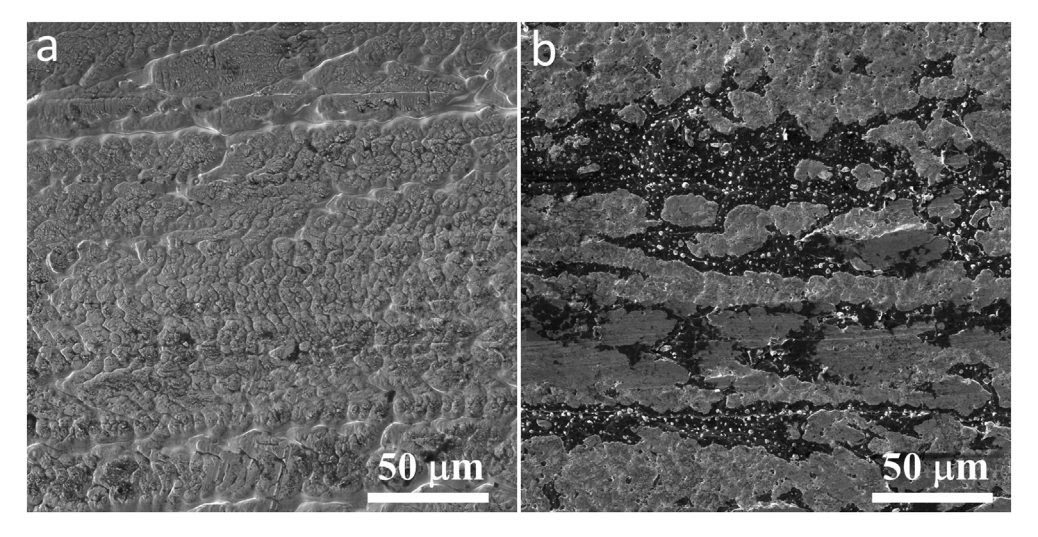


Fig. 12. (a) Plan view of as-spun Ni₈₈C₁₂ ribbon and (b) Ni₈₈C₁₂ ribbon annealed at 1000 °C for 1 h, showing the growth of carbon (black regions) on the surface post heat-treatment.

Table 1 Summary of Raman spectrum properties of freestanding carbon etched from melt spun $Ni_{92}C_8$ ribbon annealed at different temperatures.

	Before Anneal	400 °C Anneal	800 °C Anneal	1000 °C Anneal
G peak position (cm ⁻¹)	1569	1577	1571	1578
I_D/I_G	0.88	0.92	0.57	0.34
I_{2D}/I_G	0.31	0.31	0.39	0.65

Acknowledgments

This work was supported by the National Science Foundation under grant DMR-1806142.

Appendix A. Supplementary data

Supplementary data to this article can be found online at https://doi.org/10.1016/j.carbon.2021.08.037.

References

- D.M. Stefanescu, Solidification and modeling of cast iron a short history of the defining moments, Mater. Sci. Eng. 413–414 (2005) 322–333, https:// doi.org/10.1016/j.msea.2005.08.180.
- [2] K. Theuwissen, J. Lacaze, L. Laffont, Structure of graphite precipitates in cast iron, Carbon 96 (2016) 1120–1128, https://doi.org/10.1016/ j.carbon.2015.10.066.
- [3] F.J. Derbyshire, A.E.B. Presland, D.L. Trimm, Graphite formation by the dissolution-precipitation of carbon in cobalt, nickel and iron, Carbon 13 (1975) 111–113, https://doi.org/10.1016/0008-6223(75)90267-5.
- [4] K.S. Novoselov, A.K. Geim, S. V Morozov, D. Jiang, Y. Zhang, S. V Dubonos, I. V Grigorieva, A.A. Firsov, Electric field effect in atomically thin carbon films, Science 306 (2004) 666–669, https://doi.org/10.1126/science.1102896.
- [5] Q. Yu, J. Lian, S. Siriponglert, H. Li, Y.P. Chen, S.S. Pei, Graphene segregated on Ni surfaces and transferred to insulators, Appl. Phys. Lett. 93 (2008) 113103, https://doi.org/10.1063/1.2982585.
- [6] S. Amini, H. Kalaantari, J. Garay, A.A. Balandin, R. Abbaschian, Growth of graphene and graphite nanocrystals from a molten phase, J. Mater. Sci. 46 (2011) 6255–6263. https://doi.org/10.1007/s10853-011-5432-9.
- [7] L. Baraton, Z.B. He, C.S. Lee, C.S. Cojocaru, M. Châtelet, J.-L.L. Maurice, Y.H. Lee, D. Pribat, M. Chtelet, J.-L.L. Maurice, Y.H. Lee, D. Pribat, On the mechanisms of precipitation of graphene on nickel thin films, Europhys. Lett. 96 (2011) 46003, https://doi.org/10.1209/0295-5075/96/46003.
- [8] S. Amini, J. Garay, G. Liu, A.A. Balandin, R. Abbaschian, Growth of large-area graphene films from metal-carbon melts, J. Appl. Phys. 108 (2010), 094321, https://doi.org/10.1063/1.3498815.
- [9] S. Amini, R. Abbaschian, Nucleation and growth kinetics of graphene layers from a molten phase, Carbon 51 (2013) 110–123, https://doi.org/10.1016/ LCARRON 2012 08 019
- [10] A. Reina, X. Jia, J. Ho, D. Nezich, H. Son, V. Bulovic, M.S. Dresselhaus, K. Jing, Large area, few-layer graphene films on arbitrary substrates by chemical vapor deposition, Nano Lett. 9 (2009) 30–35, https://doi.org/10.1021/ pl801827y
- [11] L. Huang, Q.H. Chang, G.L. Guo, Y. Liu, Y.Q. Xie, T. Wang, B. Ling, H.F. Yang, Synthesis of high-quality graphene films on nickel foils by rapid thermal chemical vapor deposition, Carbon 50 (2012) 551–556, https://doi.org/ 10.1016/j.carbon.2011.09.012.
- [12] X. Hu, Y. Zhang, H. Ago, H. Zhou, X. Li, L. Fan, B. Cai, X. Li, M. Zhong, K. Wang, D. Wu, H. Zhu, Ultra-fast synthesis of graphene by melt spinning, Carbon 61 (2013) 299–304, https://doi.org/10.1016/j.carbon.2013.05.008.
- [13] E.H. Strange, C.A. Pim, Process of Manufacturing Thin Sheets, Foil, Strips, or Ribbons of Zinc, Lead, or Other Metal or Alloy, US905758 A, 1908. https:// www.google.com/patents/US905758. (Accessed 30 January 2018). accessed.
- [14] H. Liebermann, C. Graham, Production of amorphous alloy ribbons and effects of apparatus parameters on ribbon dimensions, IEEE Trans. Magn. 12 (1976) 921–923, https://doi.org/10.1109/TMAG.1976.1059201.
- [15] B. Cantor, W.T. Kim, B.P. Bewlay, A.G. Gillen, Microstructure cooling rate correlations in melt-spun alloys, J. Mater. Sci. 26 (1991) 1266–1276, https:// doi.org/10.1007/BF00544465.
- [16] S.R. Nishitani, K.N. Ishihara, R.O. Suzuki, P.H. Shingu, Metastable solid solubility limit of carbon in the Ni-C system, J. Mater. Sci. Lett. 4 (1985) 872–875.
- [17] K.N. Ishihara, S.R. Nishitani, H. Miyake, P.H. Shingu, Rapid solidification and the metastable phase diagrams of the Fe-C, Co-C and Ni-C systems, Int. J. Rapid Solidif. 1 (1984) 51–58.
- [18] H.H. Liebermann, The dependence of the geometry of glassy alloy ribbons on the chill block melt-spinning process parameters, Mater. Sci. Eng. 43 (1980) 203–210, https://doi.org/10.1016/0025-5416(80)90103-2.
- [19] R.E. Maringer, Solidification on a substrate, Mater. Sci. Eng. 98 (1988) 13–20, https://doi.org/10.1016/0025-5416(88)90117-6.

- [20] R.C. Ruhl, Cooling rates in splat cooling, Mater. Sci. Eng. 1 (1967) 313–320, https://doi.org/10.1016/0025-5416(67)90013-4.
- [21] H. Jones, The status of rapid solidification of alloys in research and application, J. Mater. Sci. 19 (1984) 1043–1076, https://doi.org/10.1007/BF01120015.
- [22] H.H. Liebermann, Rapidly solidified alloys made by chill block melt-spinning processes, J. Cryst. Growth 70 (1984) 497–506, https://doi.org/10.1016/ 0022-0248(84)90308-7.
- [23] W. Löser, O. Shuleshova, Nucleation and solidification kinetics of metastable phases in undercooled melts, in: D.M. Herlach, D.M. Matson (Eds.), Solidification of Containerless Undercooled Melts, Wiley, Weinheim, Germany, 2012, pp. 187–212, https://doi.org/10.1002/9783527647903.ch9.
- [24] A.G. Gillen, B. Cantor, Photocalorimetric cooling rate measurements on a Ni-5 wt% A1 alloy rapidly solidified by melt spinning, Acta Metall. 33 (1985) 1813–1825, https://doi.org/10.1016/0001-6160(85)90005-7.
- [25] I.M. Lifshitz, V.V. Slyozov, The kinetics of precipitation from supersaturated solid solutions, J. Phys. Chem. Solid. 19 (1961) 35–50, https://doi.org/10.1016/ 0022-3697(61)90054-3.
- [26] C. Wagner, Theorie der Alterung von Niederschlägen durch Umlösen (Ostwald-Reifung), Zeitschrift Für Elektrochemie, Berichte Der Bunsengesellschaft Für Phys. Chemie. 65 (1961) 581–591, https://doi.org/10.1002/BBPC.19610650704.
- [27] H. Lee, Seung Zeon Han, Hyuck Mo Lee, Z.H. Lee, Coarsening behavior of L12 precipitates in melt-spun AlTiVZr alloys, Mater. Sci. Eng. 163 (1993) 81–90, https://doi.org/10.1016/0921-5093(93)90581-X.
- [28] Z. Cai, C. Zhang, R. Wang, C. Peng, K. Qiu, N. Wang, Effect of solidification rate on the coarsening behavior of precipitate in rapidly solidified Al-Si alloy, Prog. Nat. Sci. Mater. Int. 26 (2016) 391–397, https://doi.org/10.1016/ j.pnsc.2016.08.002.
- [29] C.H. Tsau, Y.C. Chen, The coarsening of the precipitates in melt-spun Al-Ti-Zr ribbons, Mater. Chem. Phys. 73 (2002) 111–117, https://doi.org/10.1016/ S0254-0584(01)00363-7
- [30] Y.Y. Zhao, H.W. Chen, Z.P. Lu, T.G. Nieh, Thermal stability and coarsening of coherent particles in a precipitation-hardened (NiCoFeCr)94Ti2Al4 highentropy alloy, Acta Mater. 147 (2018) 184–194, https://doi.org/10.1016/ i.actamat.2018.01.049.
- [31] A. Baldan, Review Progress in Ostwald ripening theories and their applications to the γ-precipitates in nickel-base superalloys Part II Nickel-base superalloys, J. Mater. Sci. 37 (2002) 2379–2405, https://doi.org/10.1023/A:1015408116016.
- [32] E.A. Brandes, G.B. Brook (Eds.), Smithells Metals Reference Book 7th Edition, 2013. https://www.elsevier.com/books/smithells-metals-reference-book/ brandes/978-0-08-051730-8. (Accessed 2 December 2020). accessed.
- [33] D.M. Stefanescu, G. Alonso, P. Larrañaga, E. De la Fuente, R. Suarez, On the crystallization of graphite from liquid iron—carbon—silicon melts, Acta Mater. 107 (2016) 102—126, https://doi.org/10.1016/J.ACTAMAT.2016.01.047.
- [34] M.A. Pimenta, G. Dresselhaus, M.S. Dresselhaus, L.G. Cançado, A. Jorio, R. Saito, Studying disorder in graphite-based systems by Raman spectroscopy, Phys. Chem. Chem. Phys. 9 (2007) 1276–1290, https://doi.org/10.1039/B613962K.
- [35] M.S. Dresselhaus, A. Jorio, R. Saito, Characterizing graphene, graphite, and carbon nanotubes by Raman spectroscopy, Annu. Rev. Condens. Matter Phys. 1 (2010) 89–108, https://doi.org/10.1146/annurev-conmatphys-070909-103919.
- [36] A.C. Ferrari, J. Robertson, Interpretation of Raman spectra of disordered and amorphous carbon, American Physical Society (2000), https://doi.org/ 10.1103/PhysRevB.61.14095.
- [37] A.C. Ferrari, J.C. Meyer, V. Scardaci, C. Casiraghi, M. Lazzeri, F. Mauri, S. Piscanec, D. Jiang, K.S. Novoselov, S. Roth, A.K. Geim, Raman spectrum of graphene and graphene layers, Phys. Rev. Lett. 97 (2006) 187401, https:// doi.org/10.1103/PhysRevLett.97.187401.
- [38] H. Li, X. Li, J. Wei, Z. Wang, P. Guo, P. Ke, H. Saito, P. Cui, A. Wang, Crystalline transformation from ta-C to graphene induced by a catalytic Ni layer during annealing, Diam. Relat. Mater. 101 (2020) 107556, https://doi.org/10.1016/ i.diamond.2019.107556.
- [39] R.S. Weatherup, C. Baehtz, B. Dlubak, B.C. Bayer, P.R. Kidambi, R. Blume, R. Schloegl, S. Hofmann, Introducing carbon diffusion barriers for uniform, high-quality graphene growth from solid sources, Nano Lett. 13 (2013) 4264–4631, https://doi.org/10.1021/nl401601x.
- [40] G. Greenidge, J. Erlebacher, Porous graphite fabricated by liquid metal dealloying of silicon carbide, Carbon 165 (2020) 45–54, https://doi.org/10.1016/ j.carbon.2020.04.028.
- [41] S.-G. Yu, K. Yubuta, T. Wada, H. Kato, Three-dimensional bicontinuous porous graphite generated in low temperature metallic liquid, Carbon 96 (2016) 403–410, https://doi.org/10.1016/j.carbon.2015.09.093.
- [43] S. Das, Life cycle assessment of carbon fiber-reinforced polymer composites, Int. J. Life Cycle Assess. 16 (2011) 268–282, https://doi.org/10.1007/s11367-011-0264-z.